HHS Public Access

Author manuscript

*Nat Biomed Eng*. Author manuscript; available in PMC 2019 April 05.

Published in final edited form as:

*Nat Biomed Eng*. 2018 August ; 2(8): 589–599. doi:10.1038/s41551-018-0254-6.

# A designer self-assembled supramolecule amplifies macrophage immune responses against aggressive cancer

**Ashish Kulkarni**[1,3,4,*], **Vineethkrishna Chandrasekar**[1,¶], **Siva Kumar Natarajan**[1,¶], **Anujan Ramesh**[3], **Prithviraj Pandey**[5,6], **Jayashree Nirgud**[1], **Harshangda Bhatnagar**[1], **Driti Ashok**[1], **Amrendra Kumar Ajay**[1], and **Shiladitya Sengupta**[1,2,6,*]

[1]Division of Engineering in Medicine, Department of Medicine, Brigham and Women's Hospital, Harvard Medical School, Boston, MA, USA

[2]Harvard-MIT Division of Health Sciences and Technology, Cambridge, MA, USA

[3]Department of Chemical Engineering, University of Massachusetts Amherst, Amherst, MA, USA

[4]Center for Bioactive Delivery, Institute for Applied Life Sciences, University of Massachusetts, Amherst, MA, USA

[5]India Innovation Research Center, Invictus Oncology Pvt. Ltd, New Delhi, India

[6]Dana Farber Cancer Institute, Boston, MA, USA

## Abstract

Effectively activating macrophages that can 'eat' cancer cells is challenging. In particular, cancer cells secrete macrophage colony stimulating factor (MCSF), which polarizes tumour-associated macrophages from an antitumour M1 phenotype to a pro-tumourigenic M2 phenotype. Also, cancer cells can express CD47, an 'eat me not' signal that ligates with the signal regulatory protein alpha (SIRPα) receptor on macrophages to prevent phagocytosis. Here, we show that a supramolecular assembly consisting of amphiphiles inhibiting the colony stimulating factor 1 receptor (CSF-1R) and displaying SIRPα-blocking antibodies with a drug-to-antibody ratio of 17,000 can disable both mechanisms. The supramolecule homes onto SIRPα on macrophages, blocking the CD47-SIRPα signalling axis while sustainedly inhibiting CSF-1R. The supramolecule enhances the M2-to-M1 repolarization within the tumour microenvironment, and significantly improves antitumour and antimetastatic efficacies in two aggressive animal models of



[*]Correspondence to: akulkarni@engin.umass.edu; shiladit@mit.edu.
[¶]V.C. and S. N. contributed equally.

**Author Contributions:**

A.K. conceived the idea, designed the experiments and mentored the research; P. P. performed the Molecular Dynamics Simulation studies; V. C., S. N., A. R. performed the supramolecules synthesis and characterization; V. C., S. N., A. R., J. N., H. B. and D. A. performed in vitro studies; A. A. helped in confocal imaging studies; A. K., V. C., S. N. and A. R. performed in vivo experiments; A.K. and S.S. wrote the paper and received comments and edits from all the authors.

**Competing interests:**

SS is a cofounder and holds equity in Akamara Therapeutics Inc. which is developing supramolecular therapeutics.

**Data availability:**

The authors declare that all data supporting the findings of this study are available within the paper and its Supplementary Information.

melanoma and breast cancer, with respect to clinically available small-molecule and biologic inhibitors of CSF-1R signalling. Simultaneously blocking the CD47-SIRPα and MCSF-CSF-1R signalling axes may constitute a promising immunotherapy.

Macrophages form one of the first line of defense in our 'innate' immune system, and can phagocytose cancer cells[1]. However, macrophages also constitute a large fraction of the tumor stroma in nearly all cancers, and are associated with a poor prognosis[2–6]. This contradiction is explained by the existence of macrophages across a continuum of phenotypic and functional states, where the two ends of the continuum are defined as M1 and M2[7,8]. M1 macrophages mount a pro-inflammatory cytokine response, are involved in efficient antigen presentation, and promote T helper type 1 ($T_H1$) cell response, which inhibit tumor progression. In contrast, M2 macrophages are associated with a predominantly anti-inflammatory cytokine response[9]. Cancer cells create a microenvironment that is enriched in signals that skew the tumor-associated macrophages (TAMs) towards a M2-like lineage, which promotes tumor progression and metastasis, angiogenesis, and can suppress anti-tumor immune responses[3,10,11]. Depletion of TAMs, or skewing the M2 to M1 ratio towards the M1 lineage, have emerged as attractive therapeutic goals in the treatment of cancer[1,12,13]. For example, cancer cells secrete macrophage colony stimulating factor (MCSF), which drives TAM recruitment and differentiation to a M2 phenotype by binding to the tyrosine kinase CSF-receptor 1 (CSF-1R) expressed on monocytes and macrophages[11]. While inhibition of CSF-1R signaling can deplete TAMs and enable the M1 polarization, two challenges can limit the efficacy of CSF-1R inhibitors[12]. First, there is a need to inhibit CSF-1R in a temporally-sustained manner. Second, cancer cells express an 'eat me not' signal, CD47, which binds to SIRPα on macrophages and inhibits phagocytosis[14,15] (Fig. 1a), thus making a M2 to M1 switch redundant.

We rationalized that these challenges can be addressed by designing a modular bifunctional therapeutic that can block the SIRPα-CD47 interaction and simultaneously inhibit CSF-1R. Similar concepts have been used to inspire the design of bifunctional antibodies or antibody drug conjugates, where different parts of the construct have distinct functions[16,17]. In a recent study, we have demonstrated an alternative strategy, where two distinct molecular building blocks are designed to assemble into a single structure via supramolecular interactions[18] (Fig.1b). We proposed that such a supramolecule could utilize the SIRPα-targeting component for binding to macrophages and block the 'eat me not' signal, while enabling a sustained shutdown of CSF-1R-signaling pathway, which could skew the TAM M1/M2 ratio towards a M1 phenotype (Fig.1b). Together, such a bifunctional supramolecule should then result in an efficient innate immune response against the tumor.

## Computationally simulating a stable supramolecule

As the first step, we designed an amphiphilic molecular subunit that could assemble into a supramolecular structure via hydrophobic-hydrophilic interactions. In a recent study, we have described an algorithm based on quantum mechanical-all atomistic simulations to design these amphiphiles, starting from a known chemical backbone that blocked the molecular target[18,19]. The quantum mechanical energy minimized structure of an amphiphile

with a CSF-1R-inhibiting pharmacophore is shown in Fig.1c. Our previous studies have revealed that such amphiphiles form bilayers with co-lipids, resulting in a supramolecular structure in the nanoscale[18]. Unlike nanoparticles or liposomes, where the drug is loaded in a carrier matrix and are rarely stable beyond 5 mol% drug, the supramolecular assembly means that we could achieve excellent stability of the structures at >20 mol % of the amphiphile[18,19]. Indeed, an all atomistic simulation of a lipid bilayer containing 20 mol% of CSF-1R-inhibiting amphiphile revealed the formation of a stable supramolecular structure, termed AK750 (Fig. 1d). Analysis of the deuterium order parameter, i.e. ordering of the lipid tail, as a measure of stability[18], revealed that the amphiphile resulted in a lipid tail ordering that was consistent with a pure lipid bilayer (Fig.1e). We measured ripple formation as a second measure of instability, which was quantified as the 'tilt' angle between vector joining center of mass of phospholipid tails and Z-axis (axis perpendicular to bilayer plane). A tilt angle of 0° means no ripples were formed, while a broad distribution indicates a large tilt angle and high bilayer instability. As shown in Fig. 1f, the AK750 bilayer showed a narrow distribution around a tilt angle of 0°, which further validated the putative stability of the supramolecular assembly. In contrast, simulating the behavior of a classical CSF-1R inhibitor, BLZ945, in a lipid bilayer exhibited instability (Suppl. Fig.1a–b), with decreased in lipid tail ordering and broad distribution of the tilt angle as compared to the supramolecular structure (Fig.1e–f). An analysis of the position of the center of mass of the amphiphile relative to the head group of the co-lipid revealed that the pharmacophore is closer to the phospholipid head group while the hydrophobic tail anchors into the lipid bilayer, thus conferring the stability to the structure, unlike BLZ945, which sits close to the surface of the bilayer (Suppl. Fig.1c–d).

## CSF-1R-inhibiting amphiphile forms a stable supramolecule (AK750)

Based on this theoretical understanding, we next synthesized the amphiphiles by derivatizing the pharmacophore with a cholesterol anchor via a succinic acid linker (Suppl. Fig.2a–b). Consistent with the theoretic predictions, the amphiphile formed a stable supramolecular assembly with co-lipids, phosphatidylcholine and pegylated-distearoylethanolamine (PEG-DSPE). The rational for choosing the latter is that it can be derivatized with a SIRPα-blocking antibody at the terminal end of PEG, thus conferring modularity to the design of the bifunctional supramolecule. The phospholipid end co-assembles the lipid bilayer with the amphiphile. Cryo-transmission electron microscopy revealed that the supramolecular structures were spherical with a diameter of 109.4±32.7 nm (Fig.1g). Dynamic laser light scattering revealed a hydrodynamic radius of 175±15 nm, while the zeta potential was measured to be −35±7.8 mV (Fig.1h, Suppl. Fig.2c). Both size and zeta potential remained consistent over 30 days, which indicated that the supramolecular structures are indeed stable (Suppl. Fig.2c). Additionally, we observed a sustained release of the drug from the supramolecular structure when incubated with tumor cell lysate, with greater stability at physiological pH 7.4 (Suppl. Fig.2d). Indeed, as in the case of antibody drug conjugates, the stability of the construct at physiological pH and increased release in the tumor environment is a desirable characteristic that facilitates clinical success. Consistent with the computational simulation, we were unable to construct a stable nanostructure with 20 mol% of BLZ945.

## AK750 enables sustained inhibition of CSF1R signaling

Prior to introducing the SIRPα-binding functionality, we first validated that the supramolecule (AK750) indeed inhibits CSF-1R signaling. A robust and sustained activation of CSF-1R was observed in RAW-264.7 macrophage cells as early as 20 min following incubation with 10ng/ml of MCSF (Suppl. Fig.3a). We incubated the macrophages with the inhibitors for defined periods and then exposed the cells to MCSF for 20 min before analyzing the phosphorylation status of CSF-1R using Western blotting (Suppl. Fig.3b). As shown in Suppl. Fig. 3c–d, the inhibitory effects of AK750 on CSF-1R were longer-lasting compared with BLZ945. An early and late rebound phosphorylation of CSF-1R was observed with BLZ945 treatment, which could result from a feedback loop and the kinase being replenished, respectively, and is likely minimized by the sustained effect of AK750. A similar effect was observed previously with phosphatidylinositol 3 kinase (PI3K) inhibitors[20]. We next developed a string map of the direct and indirect protein interactions with CSF-1R (Fig.2a), and studied the effects of different CSF-1R inhibitors on these proteins. The macrophages were incubated with AK750, BLZ945 or PLX3397 for 4 hours, and then exposed to MCSF for 2h after a washout period of either 7 h (early time point) or 48 h (late time point) (Fig.2b). This allowed us to delineate the key pathways and dissect the persistent effects of the treatments post drug-washout. Both BLZ945 and PLX3397 are currently in the clinics for treatment of solid tumors[21]. As shown in Fig. 2c, AK750 exhibited a greater and sustained inhibition of phosphorylation of CSF-1R, and was effective in inducing a complete inhibition even at 48h. Interestingly, the downstream signaling pathway that was dominantly ablated in a sustained manner by AK750, but not by BLZ945 and PLX3397, was the AKT-mTOR-p70S6K pathway. This is consistent with recent observations that PI3K acts as a macrophage switch between immune stimulation and suppression by inhibiting macrophage inflammatory responses[21]. We did not observe any effect on the mitogen activated protein kinase signaling pathway, although it is implicated in CSF-1R signaling. Additionally, AK750 resulted in a sustained, high suppressor of cytokine signaling (SOCS) 3 to SOCS1 ratio compared with BLZ945 and PLX3397. In human tumor, expression of SOCS3 is associated with M1 polarizing environment and tumor kill, while SOCS1-expressing macrophages support tumor survival[22]. Compared with other treatments, AK750-treated macrophages also exhibited the highest inducible NOS (iNOS) to Arginase-1 ratio, which is a hallmark of M1 macrophages[23]. SOCS1 is implicated in PI3K activity, which can mediate Arginase 1 expression in M2 macrophages, while SOCS3 blocks PI3K signaling[22,24]. Additionally, RTPCR analysis revealed an increased IL12 and decreased IL10 expression in the macrophages following AK750 treatment as compared with BLZ945 and PLX3397 treatment (Suppl. Fig. 4a). These results indicated that the blockade of CSF-1R-signaling using AK750 polarizes the naïve macrophages to a M1 status.

## AK750 skews macrophage towards a M1 phenotype

Treatment with the lymphokine IL4 can polarize a macrophage to a M2 state independent of CSF1 signaling[25]. This offered the opportunity to test whether the sustained inhibition of CSF-1R afforded by AK750 could repolarize a M2 macrophage to M1-like state, which cannot be probed by current short-acting inhibitors. We incubated the macrophages with IL4 for 24 hours to skew the macrophages to an M2 state, and then added AK750 or BLZ945 for

4 h. The cells were then washed, and maintained in fresh media for 12–72h. At different time-points, we harvested the cells and analyzed the population for M1 (MHCII+, CD86+, CD80+) or M2 (CD206+) markers using fluorescence activated cell sorting (Fig. 2d). As shown in Fig. 2e–g **and** Suppl. Fig. 4–5, treatment with AK750 resulted in a significant reduction in M2 phenotype and increase in M1 macrophages as early as 12h, which was sustained even at 72 h. We did observe a reduction in M2 markers with BLZ945 at early time-points, consistent with recent findings[13], but this effect was lost at later time points. The incubation with BLZ945 did not increase the M1 markers. The FACS results were validated by Western blotting, which revealed that treatment with AK750 resulted in the highest SOCS3 to SOCS1 and iNOS to Arg-1 ratio, indicating a skew towards M1 macrophage status. Mechanistically, AK750 reduced the baseline CSF-1R activation and downstream PI3K signaling. Quantification of intracellular drug levels revealed that while both drugs reached equal levels at 4h, at 18 h we observed a higher concentration of the molecular subunit of AK750 (Suppl. Fig. 6a), which together with the sustained release of the active drug from the supramolecule can potentially explain the sustained inhibitory effects of AK750 leading to repolarization of M2 macrophages to M1.

## AK750 inhibits modulatory effects of tumor microenvironment

Cancer cells create a tumor microenvironment (TME), including secreting MCSF, which allows them to manipulate the TAMs towards a growth-enabling M2 status. Indeed, as shown in Suppl. Fig. 6b, we observed that the addition of B16/F10 melanoma-conditioned media to macrophages results in activation of CSF-1R, which is inhibited by AK750 in a sustained manner. The addition of tumor-conditioned media also decreased the iNOS signal in macrophages (Suppl. Fig. 6c), consistent with a M2 switch, which was inhibited by AK750 but not by BLZ945 (Suppl. Fig. 6d). Furthermore, quantification of iNOS to Arg-1 ratio confirmed that AK750 increased the M1 to M2 ratio despite the presence of tumor-conditioned media as compared with BLZ945 (Suppl. Fig. 6e). These results suggest that AK750 can inhibit the modulatory effects of the TME on macrophages. A similar decrease in the M2 lineage occurred when we incubated monocytes isolated from bone marrow with AK750 compared with BLZ945 in the presence of CSF1 (Suppl. Fig. 7). Neither BLZ945 nor AK750 induced any apoptosis or necrosis of macrophages or cancer cells at the concentrations used in this study (Suppl. Fig. 8a–c).

## AK750 exerts increased antitumor efficacy in melanoma and breast cancer

We next tested whether the *in vitro* observations translated into *in vivo* efficacy using two extremely aggressive, hard-to-treat syngeneic tumor models. In a recent study, we have demonstrated that supramolecular structures preferentially home into tumors, arising from the leaky pathophysiological neovasculature in the tumor. Consistent with these observations, we observed that a near-infrared dye-tagged supramolecule indeed distributed across the tumor with time (Fig.3a). Liquid chromatography-mass spectrometric (LC-MS) analysis revealed an almost 8× increase in AK750 concentration in the tumor as opposed to BLZ945 when both were administered at the same molar dose levels in animals (Fig.3b). To validate the therapeutic efficacy of AK750, we randomly sorted B16/F10 melanoma-bearing mice into three groups and treated each group with three cycles of one of the following:

blank vehicle (control); AK750; and BLZ945. The mice injected with vehicle formed large tumors by Day 10 (the day of start of treatment was considered as Day 0), and consequently were killed. The animals in the other groups were also killed at the same time point to evaluate the effect of the treatments on tumor pathology. As shown in Fig. 3c, while treatment with BLZ945 decreased tumor growth compared with vehicle-treated animals, treatment with AK750 resulted in a complete inhibition of tumor growth. Changes in body weight were within the acceptable limits (Fig.3d). Western blot analysis of the tumors lysate revealed a complete inhibition of CSF-1R phosphorylation in the tumors treated with AK750 (Fig.3e). Furthermore, quantitative analysis of the TAMs using FACS revealed that treatment with AK750 significantly reduced M2 macrophage ($CD11b^+CD206^+$) and increased the M1 pool ($CD11b^+MHCII^+$, $CD80^+$, $CD86^+$), which could mechanistically explain the *in vivo* efficacy (Fig.3f). We validated these observations in a second immunocompetent murine 4T1 breast cancer model for stage IV human breast cancer. Treatment was started when the tumors reached 75 $mm^3$ in volume (considered as Day 0). As shown in Fig.4a **and** Suppl. Fig.8d, treatment with AK750 significantly inhibited tumor growth in a dose-dependent manner. In contrast, an equimolar dose of BLZ945 had limited efficacy as did a therapeutic antibody against CSF1. The differences in response between the two tumor models is consistent with clinical observations, where melanoma responds better to immunotherapies compared to breast cancer. Interestingly, both AK750 and BLZ945 resulted in a reduction in metastatic nodes in the lungs, although the effect was significantly greater with the former (Fig.4b). This is consistent with the pro-metastatic role played by TAMs in breast cancer[10]. Additionally, treatment with AK750 significantly increased survival as compared with BLZ945 (Fig.4c). None of the treatments resulted in any change in body weight (Fig.4d). Analysis of the TAMs using FACS for M2 markers and M1 markers revealed that AK750 treatment switched the tumor macrophage from an M2 to M1 contexture. Unlike the observations in melanoma, here BLZ945 failed to reduce M2 macrophages and had no effect on M1 markers, which could explain the differences observed in efficacy outcomes with BLZ945 in the two tumor models. Interestingly, treatment with AK750 increased the number of effector $CD4/CD8^+$ T cells which are implicated in exerting a cytotoxic effect in collaboration with M1 macrophages[3,26,27] (Fig. 4e–j). Taken together, the *in vitro* and *in vivo* results indicate that the improved pharmacodynamic effect, i.e. sustained inhibition of CSF1R, and the increased intratumoral bioavailability could underlie the improved antitumor efficacy seen with AK750.

## Facile integration of SIRPα targeting to AK750

Having validated the enhanced CSF-1R-inhibiting function of AK750 compared with current clinical approaches of targeting CSF1 signaling, we next tested whether integrating the SIRPα-targeting function to the supramolecule can further increase the anti-tumor efficacy over and above that seen with AK750. The modularity of the system meant that we could display SIRPα-blocking antibodies on the surface of the supramolecule via simple conjugation to the terminal ends of the polyethylene glycol chains using a carbodiimide cross-linker chemistry. Theoretically, the surface area of a spherical supramolecule of ~100 nm diameter is ~30000 $nm^2$, which means it can accommodate ~150 antibodies aligned parallel to each other (Fig.5a). As the first step, we engineered the anti-SIRPα-AK750

supramolecules with increasing number of antibodies (Fig.5b) while keeping the concentration of the CSF-1R-inhibiting amphiphiles per supramolecule constant. An analysis based on the average number of supramolecules in an aliquot indicated that each supramolecule is comprised of approximately 425000±149000 molecules of the CSF-1R-inhibiting amphiphiles. Integrating between 10 to 94 antibodies per supramolecule (318–2993 antibodies/$\mu m^2$), while keeping the concentration of AK750 constant, resulted in a drug antibody ratio (DAR) ranging between ~4521 to 40476 (Fig.5c). This is a significant improvement over classical ADCs, that typically have a DAR of 4–6[28]. We next tested the impact of this increasing antibody density on the phagocytosis of cancer cells by macrophages. The anti-SIRPα-AK750 supramolecules, with increasing number of SIRPα-blocking antibodies, were added to a co-culture of macrophages and cancer cells. As shown in Fig. 5d, a bell-shaped concentration-efficacy (phagocytosis) curve was obtained, with maximal phagocytosis achieved at a density of 541 antibodies/$\mu m^2$. The degree of phagocytosis was statistically similar between 541 antibodies/$\mu m^2$ and 796 antibodies/$\mu m^2$ but decreased at 1624 antibodies/ $\mu m^2$, which could arise from steric hindrances. We conducted further studies with supramolecules with 796 antibodies/$\mu m^2$, which translated to 25 ± 9 antibodies/supramolecule, based on the rationale that a higher antibody coverage increases the probability of binding in a dynamic system. The total incorporation efficiency of the CSF-1R-inhibiting amphiphile in the anti-SIRPα-AK750 supramolecule was calculated to be 76±5%, statistically not different from that achieved in the case of the AK750 supramolecule (83 ± 2%) (Suppl. Fig. 9a), consistent with the modularity of the system that allows addition of functionality without impacting the basic composition. The hydrodynamic diameter of this bi-functional supramolecule was found to increase marginally to ~180 ± 27 nm (Suppl. Fig. 9b). The surface charge (zeta potential) was calculated to be −17±8 mV. Neither size nor surface charge varied significantly over a 7-day period indicating that the bifunctional supramolecules are stable (Suppl. Fig. 9c). Furthermore, less than 20% of the total CSF-1R-inhibiting amphiphile was found to be released over the study period at physiological pH 7.4, consistent with that observed earlier in the case of AK750 supramolecules. In contrast, a sustained, >80% release was observed when the supramolecules were incubated with macrophage cell lysate (Suppl. Fig. 9d). To test the serum stability, we incubated the anti-SIRPα-AK750 supramolecule in increasing concentration of human serum and quantified the change in diameter over time. No statistical change in diameter was observed over 24 hours, but a serum concentration-dependent increase was evident at later time points, consistent with corona formation (Suppl. Fig. 9e).

## Enhanced binding of the anti-SIRPα-AK750 to macrophages

To validate whether the bifunctional supramolecule binds to SIRPα on macrophages, we incubated TAMs isolated from B16/F10 melanoma-bearing mice with anti-SIRPα-AK750 or control IgG-AK750 that were fluorophore-tagged. At the end of 4 hours of incubation, the cells were washed with cold PBS and analyzed using flow cytometry, which revealed significantly enhanced binding of the anti-SIRPα-AK750 as compared to control IgG-AK750 (Fig.5e). Additionally, immunolabeling the TAMs for SIRPα followed by fluorescence microscopy revealed a colocalization of the signals from fluorophore-tagged

anti-SIRPα-AK750 and SIRPα (Fig.5f), which further validated the binding of the supramolecule to SIRPα. To test whether the anti-SIRPα-AK750 blocks the SIRPα-CD47 axis, we treated melanoma cells with interferon gamma (IFNγ) to increase the expression of CD47, and then added fluorescently tagged SIRPα to the cells in the presence of anti-SIRPα-AK750 or control IgG-AK750. Confocal imaging revealed that the treatment with anti-SIRPα-AK750 completely inhibited the SIRPα-CD47 binding unlike the control IgG-AK750 supramolecules (Fig.5g–h). Ligation to SIRPα can potentially inhibit phagocytosis[14]. Given that cellular internalization is critical for the anti-SIRPα-AK750 to inhibit CSF-1R, we next tested whether the binding to SIRPα inhibits the internalization of the supramolecule into the cell. As shown in Fig.5i, we observed greater internalization within the macrophages within 4 hours of incubation as compared with a control IgG-coupled AK750. Furthermore, Western blotting revealed a significant inhibition of phosphorylation of CSF-1R in macrophages treated with anti-SIRPα-AK750 (Fig.5j).

## Anti-SIRPα-AK750 increases phagocytosis of cancer cells and anticancer efficacy

We next tested whether the anti-SIRPα-AK750 treatment results in a greater antitumor effect than AK750 *in vivo* using the aggressive B16/F10 melanoma model. As three cycles of AK750 maximally ablated tumor growth, we first treated tumor-bearing animals with two cycles of treatment. At this dose, AK750 submaximally inhibited tumor growth. The integration of the anti-SIRPα activity to the AK750 supramolecules significantly increased the anti-tumor efficacy as compared with AK750 or BLZ945 treatments (Fig.6a). Analyzing the TAMs revealed that the treatment with anti-SIRPα-AK750 significantly increased the M1 phenotype as compared with AK750 treatment (Fig.6b). Interestingly, the bifunctional anti-SIRPα-AK750 exerted a greater anticancer efficacy than a combination of SIRPα-blocking antibody and AK750 (Suppl. Fig. 10a). We used a dose of 5mg/kg for the anti-SIRPα antibody, which for a mouse of 20g translates to ~ $4 \times 10^{14}$ molecules. Similarly, we injected AK750 equivalent to ~ $1.3 \times 10^{18}$ molecules of the CSF1-R-inhibiting amphiphile/20g mouse. The dosing of anti-SIRPα-AK750 translated to ~ $1.3 \times 10^{18}$ molecules of the amphiphile and $7.5 \times 10^{13}$ antibodies (based a DAR of 17000). One should note that a classical ADC-based approach using the same number of anti-SIRPα antibody as used in the anti-SIRPα-AK750 would have translated to ~ $1.5 \times 10^{14}$ (at DAR of 2) – $1.5 \times 10^{14}$ (at DAR of 6) molecules of the CSF-1R-inhibitor, which is significantly lower than ~ $1.3 \times 10^{18}$ molecules that was achieved with the supramolecular approach. A lower amount of antibody is therefore able to exert a greater effect when engineered together with the CSF-1R-inhibiting amphiphile in the same supramolecular construct as opposed to a combination of two separate entities. This is consistent with our recent observations, where bifunctional 2-in-1 supramolecules exerted greater efficacy than the simple combinations of two therapeutic agents. We demonstrated that two therapeutic agents can stochastically distribute within the tumor independent of each other such that subsets of target cells are exposed to only one of the therapeutic agents, which lowers the total efficacy. In contrast, bifunctional 2-in-1 supramolecules ensure that both therapeutic agents are presented to the same cell[29]. Additionally, we rationalized that the anti-SIRPα component could confer a tumor-homing functionality to the supramolecule. To test this, we next performed biodistribution studies,

where animals were injected with AK750 or anti-SIRPα-AK750, and the levels of AK750 in different tissues was detected using LCMS. As shown in Fig.6c, anti-SIRPα-AK750 treatment resulted in a significantly greater build-up of the drug in the tumor at an early time-point (8h) as compared with AK750. While this distinction between AK750 and anti-SIRPα-AK750 was lost at a late time-point, the total intratumoral drug concentration reached with the anti-SIRPα-AK750 was two-fold that reached with AK750 within 36h. Both treatments resulted in greater intra-tumoral concentrations than BLZ945. Furthermore, pharmacokinetic studies revealed that unlike AK750, the anti-SIRPα-AK750 exhibited a bell-shaped plasma concentration-time curve, suggestive of a reservoir to which the anti-SIRPα-supramolecule binds at earlier time-point. Taken together with the biodistribution data, this result is consistent with the binding of anti-SIRPα-AK750 to circulating and tumor macrophages/monocytes, which could also explain the longer half-life (Suppl. Fig. 10b–c). The delayed accumulation of AK750 in the tumor is consistent with the ability of nanoparticles to passively home into tumors over time due to an enhanced permeability and retention effect[30]. Based on the pharmacokinetic studies, we rationalized the synergistic anti-cancer effect seen with the bifunctional anti-SIRPα-AK750 over AK750 can be best dissected with a single dose of the drug as repeat dosing within short time-intervals could result in saturation kinetics, where the CSF-1R inhibition could mask the impact of the SIRPα inhibition. Indeed, as shown in Fig. 6d, a single dose of anti-SIRPα-AK750 resulted in a dramatic inhibition of tumor progression. In contrast, a single dose of anti-SIRPα antibody had minimal effect on the tumor progression, while the single dose of control IgG-AK750 resulted in an initial delay in tumor progression with tumor rebound seen at later time points. None of the treatments resulted in any off-target toxicity to the organs studied, as quantified using TUNEL staining that labels apoptotic cells (Fig.6d2, Suppl. Fig.10d). We did not see depletion of $F4/80^+$ cells in the tumors treated with anti-SIRPα-AK750 as compared to vehicle control, consistent with recent observations (Fig.6d1).[31] To further understand the increased efficacy with anti-SIRPα-AK750 at a mechanistic level, we loaded B16/F10 melanoma cells with a cell-impermeant CFSE dye and incubated them for 8 hours with macrophages that were pretreated with the supramolecules or BLZ945. As shown in Fig. 6e–f, treatment with anti-SIRPα-AK750 significantly increased the phagocytosis of cancer cells by macrophages as compared with either IgG-AK750 or BLZ945 treatments. Additionally, the treatments exerted a direct inhibitory effect on the tumor cells only at very high concentrations exceeding the levels we used for the study (Suppl. Fig. 11a–b). However, even at the highest concentrations, we did not observe any significant apoptosis of macrophages (Suppl. Fig.11c). Taken together, these results indicate that anti-SIRPα component of anti-SIRPα-AK750 can facilitate the targeting of TAMs; The inhibition of the ‘eat me not’ signal synergizes with the repolarization of TAMs to the M1-phenotype resulting from CSF-1R inhibition to exert enhanced anticancer effects compared with AK750 treatment alone.

Several components of the bifunctional supramolecule can advance immunotherapy in humans. First, the ability of the supramolecules to accumulate in the tumor, resulting from increased bioavailability, together with the homing to SIRPα on the TAMs, could result in greater intratumoral concentrations and minimize off-target toxicity, and translate into an improved therapeutic index. Second, the supramolecule induces a sustained inhibition of

CSF-1R and key downstream signaling cascades, resulting in enhanced antitumor efficacy and reduced metastasis in aggressive tumor models compared with current clinical-stage inhibitors of MCSF-CSF-1R axis. Third, it is increasingly being realized that combination immunotherapy, including blocking two distinct targets in the same immune cell, is the future of immunooncology. For example, in recent clinical studies, targeting programmed cell death protein 1 (PD1) and cytotoxic T-lymphocyte-associated protein 4 (CTLA4) on T cells with the combination of a standard dose of pembolizumab together with a reduced dose of ipilimumab, respectively, was found increase anticancer efficacy without amplifying the side effects[32]. Our results with the SIRPα-AK750 supramolecule lays the groundwork for a combination approach targeting both CD47-SIRPα and MCSF-CSF-1R signaling axes simultaneously, rather than targeting a single axis, to maximally activate macrophages in immunooncology. The fact that a single cycle of the SIRPα-AK750 supramolecule exerted significant tumor inhibition suggests that such an approach may allow the reduction in total dose without losing efficacy. Although the supramolecules induce a dramatic repolarization of TAMs from an M2 to M1 phenotype, associated increase in phagocytosis of cancer cells, and enhanced antitumor efficacy, it is likely that the macrophage-activating supramolecules will have to be combined with immune checkpoint inhibitors that can enable T cells to respond efficiently to antigen presentation by macrophages. Such an integrative immunotherapy approach underpinned by bifunctional supramolecules can emerge as a new paradigm in the treatment of cancer.

## Methods

Detailed methods are described in supplementary information.

### Synthesis and characterization of anti-SIRPα-AK750

CSF-1R inhibiting amphiphile was synthesized by conjugating BLZ945 with cholesteryl hemisuccinate using EDC and DMAP coupling reaction as described in the supplementary methods. The products were characterized by $^{1}$H NMR spectroscopy and mass spectrometry. For supramolecule synthesis, 20 mol % of CSF-1R inhibiting amphiphile, 30 mol % 1,2-distearoyl-*sn*-glycero-3-phosphoethanolamine-N-[carboxy(polyethylene glycol)-2000] and 50 mol % L-α-phosphatidylcholine was dissolved in 1ml of DCM. The solvent was evaporated into a thin and uniform film using a rotary evaporator. The film was then hydrated with 1.0 ml $H_2O$ for 1.5 h at 60°C. After hydration, 1 equivalent of EDC and NHS were each added and incubated at room temperature for 2 hours. To the samples, 4 μl (0.5mg/kg concentration) of either IgG (control) or anti-SIRPα antibodies were added and the samples were incubated at 4°C for 12h. We used a well-characterized anti-SIRPα blocking IgG antibody (BioLegend, AB_11203723). After incubation, the samples were extruded at 60 °C using a 400 nm and then 200 nm PC membrane with 500 μl sample volume to obtain sub-200 nm particles. The samples were further passed to Sephadex G-25 column to remove free molecular subunits and non-conjugated antibodies. The physical stability of the nanoparticles was evaluated by measuring changes in mean particle size and ζ potential during storage condition in 4°C.

### Quantum mechanical all-atomistic simulations

An all atomistic simulation was performed to elucidate the stability of the supramolecular structures. Briefly, geometry optimization using quantum mechanical (QM) methods was performed to obtain the lowest energy conformation of the molecular subunit or BLZ945. Following the force field development step, the subunit was energy optimized using the developed force field using steepest descent algorithm. QM geometry-optimized structures of were considered as the starting structure for MD simulations. BLZ945 and CSF-1R inhibiting molecular subunit molecules were inserted inside the lipid bilayer structure and equilibrated till 10ns for all the systems to randomize. Models were constructed such that the system contained 256 molecules of co-lipid and 64 molecules of geometry-optimized structure of molecular subunit. The trajectories were analyzed as described in supplementary information.

### In vitro macrophage polarization assays

The supramolecules were tested on both primary and cell line cultures, *in vitro,* under different conditions described in supplementary information. The efficacy was quantified using Western blotting or flow cytometry.

### In-vitro phagocytosis assay

$5 \times 10^4$ RAW264.7 Cells were plated per well in an 8-well chamber slide. After 24h of IL-4 (20ng/mL) stimulation, anti-Sirpα-AK750, AK750, IgG-AK750, and BLZ945 free drug were added at 67nM (equivalent to BLZ-945 conc.) to macrophages and incubated for 3 hours at 37°C. The macrophages were labeled with APC anti- CD11b antibody. B16/F10 melanoma cells ($5\times10^4$) were labeled with CFSE as per manufacturer's protocol and added to macrophages at 1:1 ratio and incubated for 8h. The imaging was performed with an Olympus Confocal microscope. The images were analyzed and quantification was performed using ImageJ software.

### In vivo efficacy studies

B16/F10 Melanoma cells ($1 \times 10^5$) or 4T1 cells were implanted subcutaneously in the flanks of 4–6 weeks old C57BL/6 mice or female balb/c mice respectively (Charles River Laboratories). When the tumor volume reached a predefined size (~ 50 $mm^3$), the animals were randomized into different treatment groups. The animals were administered *via* tail vain with following treatments as described in supplementary information. The tumor volume was calculated by using the formula, $L \times B^2/2$, where the L and B are the longest diameter and the shortest diameter, respectively, as measured using a vernier caliper. Animals were sacrificed once the tumors in the vehicle-treated group reached a predetermined cut-off or sign of any distress. The tumor tissues were harvested for further immune characterization. All animal procedures were approved by the Harvard Institutional Use and Care of Animals Committee.

## Supplementary Material

Refer to Web version on PubMed Central for supplementary material.

## Acknowledgments

This work was supported by a DoD Breakthrough Award (BC132168), an American Lung Association Innovation Award (LCD-259932-N), and an NCI UO1 (CA214411) to S.S. and a National Cancer Institute of the National Institutes of Health (P50CA168504) and Hearst Foundation/Brigham & Women's Hospital Young Investigator Award to A. K. The authors would like to thank the Dana Farber Cancer Institute Flow Cytometry Core Facility for their expertise, consulting and assistance with flow cytometry experiments. The authors would like to thank the Mass Spectrometry Core Facility and Biophysical Characterization Core Facility at the Institute for Applied Life Sciences (IALS), University of Massachusetts Amherst for their consulting and assistance in Mass Spectrometry experiments.

## References

1. Mantovani A, Marchesi F, Malesci A, Laghi L, Allavena P. Tumour-associated macrophages as treatment targets in oncology. Nature reviews. Clinical oncology. 2017
2. Engblom C, Pfirschke C, Pittet MJ. The role of myeloid cells in cancer therapies. Nature reviews. Cancer. 16:447–462. DOI: 10.1038/nrc.2016.542016; [PubMed: 27339708]
3. Noy R, Pollard JW. Tumor-associated macrophages: from mechanisms to therapy. Immunity. 41:49–61. DOI: 10.1016/j.immuni.2014.06.0102014; [PubMed: 25035953]
4. Condeelis J, Pollard JW. Macrophages: obligate partners for tumor cell migration, invasion, and metastasis. Cell. 124:263–266. DOI: 10.1016/j.cell.2006.01.0072006; [PubMed: 16439202]
5. Gabrilovich DI, Ostrand-Rosenberg S, Bronte V. Coordinated regulation of myeloid cells by tumours. Nature reviews. Immunology. 12:253–268. DOI: 10.1038/nri31752012;
6. Grivennikov SI, Greten FR, Karin M. Immunity, inflammation, and cancer. Cell. 140:883–899. DOI: 10.1016/j.cell.2010.01.0252010; [PubMed: 20303878]
7. Biswas SK, Mantovani A. Macrophage plasticity and interaction with lymphocyte subsets: cancer as a paradigm. Nature immunology. 11:889–896. DOI: 10.1038/ni.19372010; [PubMed: 20856220]
8. Mosser DM, Edwards JP. Exploring the full spectrum of macrophage activation. Nature reviews. Immunology. 8:958–969. DOI: 10.1038/nri24482008;
9. Sica A, et al. Macrophage polarization in tumour progression. Seminars in cancer biology. 18:349–355. DOI: 10.1016/j.semcancer.2008.03.0042008; [PubMed: 18467122]
10. Qian BZ, Pollard JW. Macrophage diversity enhances tumor progression and metastasis. Cell. 141:39–51. DOI: 10.1016/j.cell.2010.03.0142010; [PubMed: 20371344]
11. Ruffell B, Coussens LM. Macrophages and therapeutic resistance in cancer. Cancer cell. 27:462–472. DOI: 10.1016/j.ccell.2015.02.0152015; [PubMed: 25858805]
12. Ries CH, et al. Targeting tumor-associated macrophages with anti-CSF-1R antibody reveals a strategy for cancer therapy. Cancer cell. 25:846–859. DOI: 10.1016/j.ccr.2014.05.0162014; [PubMed: 24898549]
13. Pyonteck SM, et al. CSF-1R inhibition alters macrophage polarization and blocks glioma progression. Nature medicine. 19:1264–1272. DOI: 10.1038/nm.33372013;
14. Chao MP, Weissman IL, Majeti R. The CD47-SIRPαlpha pathway in cancer immune evasion and potential therapeutic implications. Current opinion in immunology. 24:225–232. DOI: 10.1016/j.coi.2012.01.0102012; [PubMed: 22310103]
15. McCracken MN, Cha AC, Weissman IL. Molecular Pathways: Activating T Cells after Cancer Cell Phagocytosis from Blockade of CD47 "Don't Eat Me" Signals. Clinical cancer research : an official journal of the American Association for Cancer Research. 21:3597–3601. DOI: 10.1158/1078-0432.CCR-14-25202015; [PubMed: 26116271]
16. Beck A, Goetsch L, Dumontet C, Corvaia N. Strategies and challenges for the next generation of antibody-drug conjugates. Nature reviews. Drug discovery. 16:315–337. DOI: 10.1038/nrd.2016.2682017; [PubMed: 28303026]
17. Garber K. Bispecific antibodies rise again. Nature reviews. Drug discovery. 13:799–801. DOI: 10.1038/nrd44782014;
18. Kulkarni A, et al. Algorithm for Designing Nanoscale Supramolecular Therapeutics with Increased Anticancer Efficacy. ACS nano. 10:8154–8168. DOI: 10.1021/acsnano.6b002412016; [PubMed: 27452234]

19. Kulkarni A, Natarajan SK, Chandrasekar V, Pandey PR, Sengupta S. Combining Immune Checkpoint Inhibitors and Kinase-Inhibiting Supramolecular Therapeutics for Enhanced Anticancer Efficacy. ACS nano. 2016
20. Kulkarni. Cancer Res. 2013
21. Zhou D, et al. Macrophage polarization and function with emphasis on the evolving roles of coordinated regulation of cellular signaling pathways. Cellular signalling. 26:192–197. DOI: 10.1016/j.cellsig.2013.11.0042014; [PubMed: 24219909]
22. Wilson HM. SOCS Proteins in Macrophage Polarization and Function. Frontiers in immunology. 5:357.2014; [PubMed: 25120543]
23. Ruffell B, Affara NI, Coussens LM. Differential macrophage programming in the tumor microenvironment. Trends in immunology. 33:119–126. DOI: 10.1016/j.it.2011.12.0012012; [PubMed: 22277903]
24. Whyte CS, et al. Suppressor of cytokine signaling (SOCS)1 is a key determinant of differential macrophage activation and function. Journal of leukocyte biology. 90:845–854. DOI: 10.1189/jlb.11106442011; [PubMed: 21628332]
25. Genin M, Clement F, Fattaccioli A, Raes M, Michiels C. M1 and M2 macrophages derived from THP-1 cells differentially modulate the response of cancer cells to etoposide. BMC cancer. 15:577.2015; [PubMed: 26253167]
26. Gajewski TF, Schreiber H, Fu YX. Innate and adaptive immune cells in the tumor microenvironment. Nature immunology. 14:1014–1022. DOI: 10.1038/ni.27032013; [PubMed: 24048123]
27. Ruffell B, et al. Macrophage IL-10 blocks CD8+ T cell-dependent responses to chemotherapy by suppressing IL-12 expression in intratumoral dendritic cells. Cancer cell. 26:623–637. DOI: 10.1016/j.ccell.2014.09.0062014; [PubMed: 25446896]
28. Diamantis N, Banerji U. Antibody-drug conjugates--an emerging class of cancer treatment. British journal of cancer. 114:362–367. DOI: 10.1038/bjc.2015.4352016; [PubMed: 26742008]
29. Goldman A, et al. Rationally Designed 2-in-1 Nanoparticles Can Overcome Adaptive Resistance in Cancer. ACS nano. 10:5823–5834. DOI: 10.1021/acsnano.6b003202016; [PubMed: 27257911]
30. Sengupta S. Cancer Nanomedicine: Lessons for Immuno-Oncology. Trends Cancer. 3:551–560.2017; [PubMed: 28780932]
31. Gholamin S, et al. Disrupting the CD47-SIRPαlpha anti-phagocytic axis by a humanized anti-CD47 antibody is an efficacious treatment for malignant pediatric brain tumors. Science translational medicine. 92017;
32. Long GV, et al. Standard-dose pembrolizumab in combination with reduced-dose ipilimumab for patients with advanced melanoma (KEYNOTE-029): an open-label, phase 1b trial. Lancet Oncol. 18:1202–1210. DOI: 10.1016/S1470-2045(17)30428-X2017; [PubMed: 28729151]

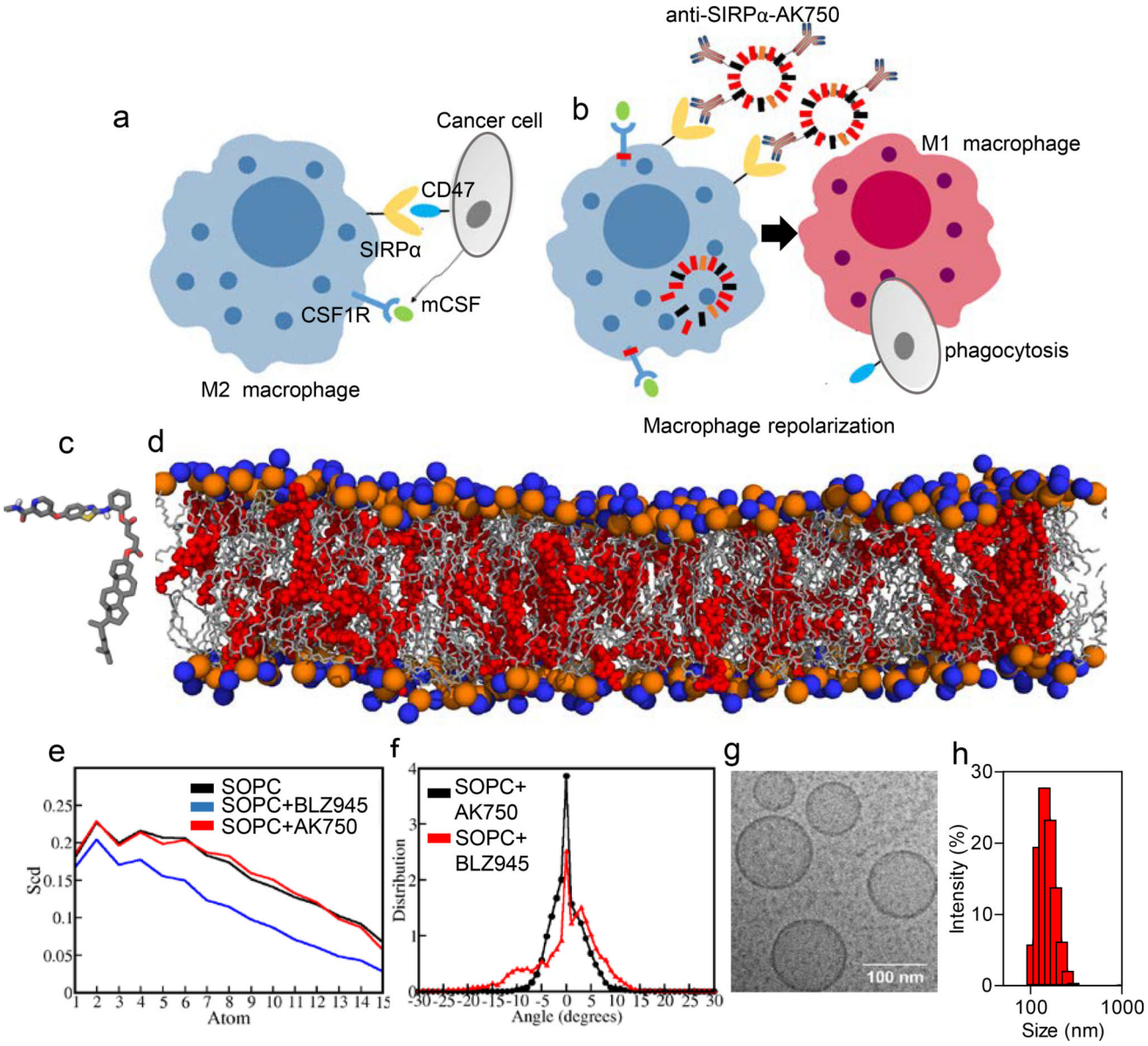


**Figure 1. Design of a TAM-targeting supramolecular therapeutic**

**(a)** Schematic shows that cancer cells exploit colony stimulating factor 1 receptor (CSF-1R) signaling to polarize macrophages to immunosuppressive “M2” phenotype, and signal regulatory protein alpha (SIRPα)-CD47 interactions to inhibit phagocytosis. **(b)** Schematic illustration of efficient repolarization of M2 macrophage to effector “M1” phenotype by dual-function supramolecular therapeutic (anti-SIRPα-AK750)-mediated sustained inhibition of CSF-1R signaling and enhanced phagocytosis of cancer cells following inhibition of SIRPα. **(c)** Representation of the QM-optimized structure of the molecular subunit of supramolecular nanostructure, AK750. **(d)** Snapshot of all atomistic simulation of the molecular subunit (in red) interacting with the lipid bilayer at 100ns shows stable supramolecular structure; Lipid (SOPC) hydrophilic heads are shown in orange and blue spheres and lipid tails are shown in grey color. **(e)** Angle between vector defined on C-C

bond on SOPC tail with Z-axis (axis perpendicular to bilayer plane) is depicted as θ. Deuterium order parameter (Scd) is calculated using θ. Scd is calculated on each carbon atom of phospholipid tail. Higher the -Scd, higher is the lipid tail ordering; Deuterium order parameter on each methylene group on saturated tail of co-lipid is depicted. Lipid tail ordering for BLZ945-containing lipid bilayer is the least. Lipid tail ordering of AK750 bilayer is similar to that of the pure lipid bilayer; **(f)** Tilt angle is the angle between vector joining center of mass of phospholipid tails and Z-axis (axis perpendicular to bilayer plane). Value of tilt angle is positive or negative depending on direction of the ripple. Its value is close to 0° when no ripples form. Distribution of tilt angle averaged over last 5 ns of MD trajectory. Broader the distribution larger is the tilt angle, higher is the extent of bilayer instability. **(g)** High resolution cryo-TEM image of AK750 showing size of ~100 nm and spherical morphology; **(h)** Graph shows the size distribution (hydrodynamic diameter) of a representative batch of AK750 as measured by dynamic light scattering. The description of panels **c–g** is adapted from ref. 19.

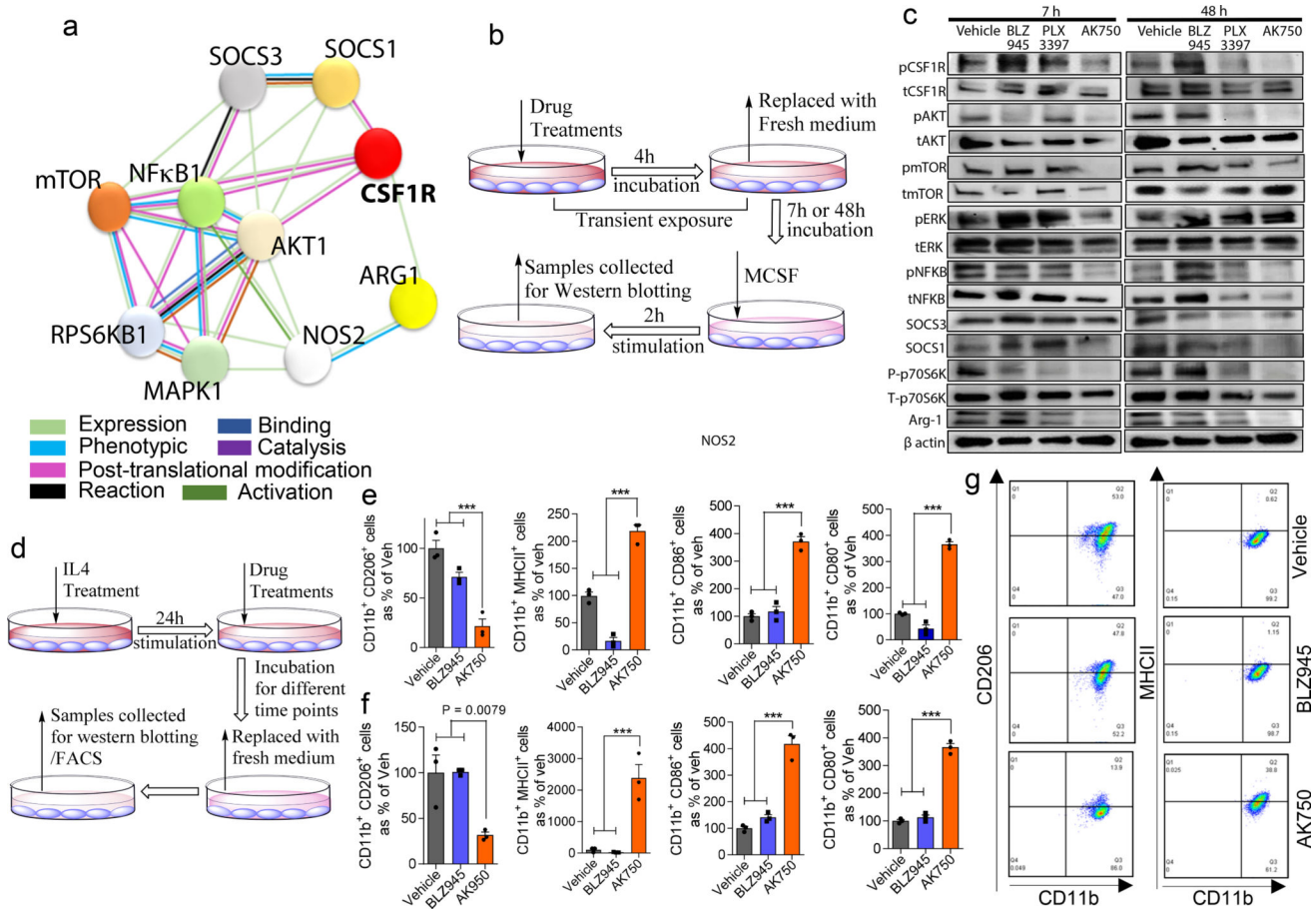


**Figure 2. AK750 inhibits CSF-1R and downstream signaling pathways in a sustained manner, and efficiently repolarize M2 macrophages to M1 phenotype**

**(a)** STRING map showing different direct or indirect protein interactions associated with CSF-1R signaling pathway in macrophages. The STRING map was generated by using STRING database version 10.0; **(b)** Schematic representation of CSF-1R pathways inhibition assay. RAW264.7 macrophage cells were pre-treated with either BLZ945, PLX3397 or AK750 for 4h, and then washed with cold PBS to remove the drugs that are not internalized. After 7h or 48h of recovery in fresh medium, the cells were stimulated with either MCSF for 2h. The cells were then washed and analyzed for activation of signaling pathway as shown in **(c)** Western blot for phosphor-CSF-1R, total CSF-1R and downstream signaling pathways. The cropped blots are used in the figure, and full-length blots are presented in Supplementary Fig. 13; **(d)** Schematic representation of macrophage repolarization assay. RAW264.7 macrophages were stimulated with IL4 for 24h, and then treated with either BLZ945, PLX3397 or AK750 for 12h before replacing with fresh medium. The cell lysates were collected at different timepoints for western blotting and FACS; **(e–f)** Quantification of flow cytometry data demonstrating expression of M2 markers (CD11b+CD206+), or M1 markers (CD11b+, MHC-II, CD86+ CD80+). The data shown are at **(e)** 12h, and **(f)** 72h time points. Statistical analysis was performed with One-way ANOVA with Newman-Keuls post Test. Data shows mean ± SEM (n = 3); ***p < 0.001; **(g)** Flow cytometry demonstrating expression of CD11b+CD206+, CD11b+MHC-II+, CD11b

+CD86+ and CD11b+CD80+ on the macrophages at 72h time point following different treatments.

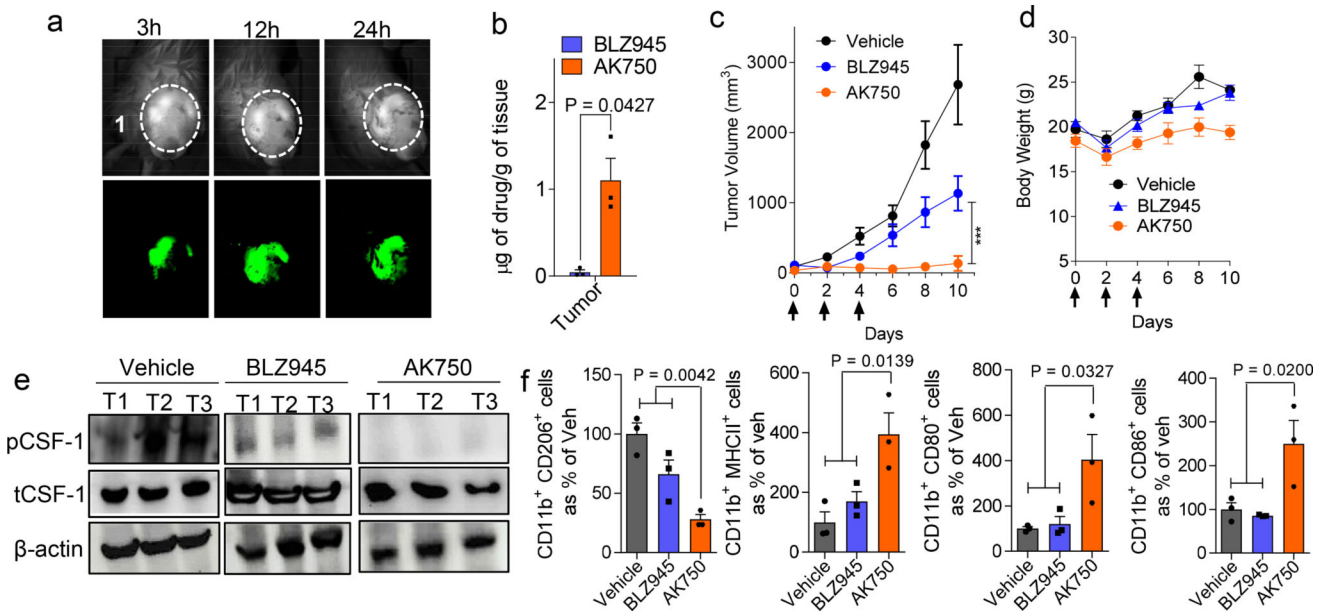


**Figure 3.** ***In vivo*** **efficacy of AK750 in a syngeneic B-16/F10 melanoma C57BL/6 mice model**

**(a)** Representative image shows the temporal accumulation of a NIR dye-tagged AK750 in the tumor in a melanoma-bearing mouse model. **(b)** Graph shows the quantification of actual drug concentration reached in the tumor, in vivo, as measured using LC-MS. Tumor-bearing animals were injected with equimolar dose of the drugs. Data shows mean ± SEM (n = 3), *p < 0.05 (Student's t-test, two-sided). **(c)** Tumor growth curves show effect of different treatments on tumor volume. Each animal was injected with three doses of either vehicle (for control group), 45 mg/kg of free BLZ945, and AK750 (at equimolar dose to BLZ945) on day 0, day 4 and day 8. First day of treatment was considered as Day 0. Treatment with AK750 was significantly more effective than BLZ945. One should note the different routes of administration, and i.p. administration can result in lower bioavailability than i.v. administration. Data shown are mean ± SEM (n = 5), ***p < 0.001 (One-way ANOVA). **(d)** Graph shows drug toxicity assessed by measurements in overall body weight. Data shown are mean ± SEM (n = 5). **(e)** Western blot shows expression of phosphor-CSF-1R and total CSF-1R in 3 representative tumors in each treatment group, in vivo. The cropped blots are used in the figure, and full-length blots are presented in Supplementary Fig. 14; **(f)** Graphs show the quantification of expression of different M2 markers (CD11b+CD206+), or M1 markers (CD11b+MHC-II+, CD11b+CD86+ and CD11b+CD80+) in single cell suspension of the harvested tumor post-treatment, as quantified using flow cytometry. Tumors were harvested on day 10 and single cell suspension was prepared. Data shown are mean ± SEM (n = 3), p values are shown in the graphs. Statistical analysis was performed with One-way ANOVA with Newman-Keuls post Test.

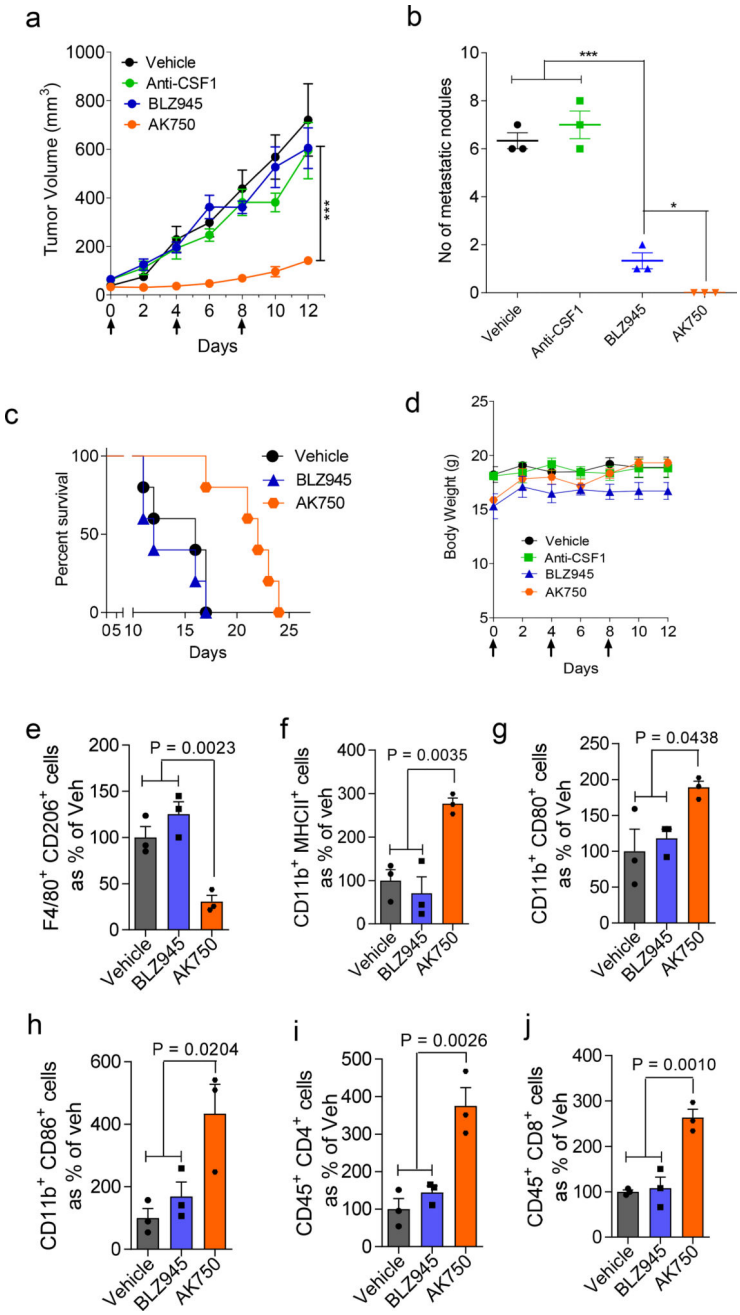


**Figure 4. AK750 induces significant tumor growth inhibition in a syngeneic 4T1 breast cancer BALB/c mice model**

**(a)** Growth curves show effect of different multi-dose treatments on tumor volume in 4T1 tumor bearing mice Tumor growth curves show effect of different treatments on tumor volume. Each animal was injected with three doses of either vehicle (for control group), 45 mg/kg of free BLZ945, AK750 (at equimolar dose to BLZ945) or a CSF-1 neutralizing antibody (25mg/kg) on day 0, day 4 and day 8. First day of treatment was considered as Day 0. Data shown are mean ± SEM (n = 5), ***p < 0.001 (One-way ANOVA). **(b)** Graph shows the number of metastatic nodules present in the lungs. Lungs were harvested from treated tumor-bearing mice on day 12, washed with cold PBS, and the number of metastatic nodules

were counted. BLZ945 showed a reduction as compared to CSF-1 neutralizing antibody and the vehicle control, However the AK750 displayed complete inhibition of formation of metastatic nodules. Data shown are mean ± SEM (n = 3), *p < 0.05; ***p < 0.001 (ANOVA followed by Newman Keul's Post hoc test). **(c)** Kaplan Meir survival curves show that treatment with AK750 increases survival (P<0.05) as compared with BLZ945 (n=5 in each treatment group). One should note the different routes of administration, and i.p. administration can result in lower bioavailability than i.v. administration. **(d)** Graph shows drug toxicity assessed by measurements in overall body weight. Data shown are mean ± SEM (n = 5). **(e–j)** Graphs show the quantification of expression of different M2 markers (CD11b+CD206+), M1 markers (CD11b+MHC-II+, CD11b+CD86+ and CD11b+CD80+), and effector T cell markers (CD45+CD4+, CD45+CD8+) in single cell suspension of the harvested tumor post-treatment, as quantified using flow cytometry. Tumors were harvested on day 12 and single cell suspension was prepared. Data shown are mean ± SEM (n = 3), p values are shown in the graphs. Statistical analysis was performed with One-way ANOVA with Newman-Keuls post Test.

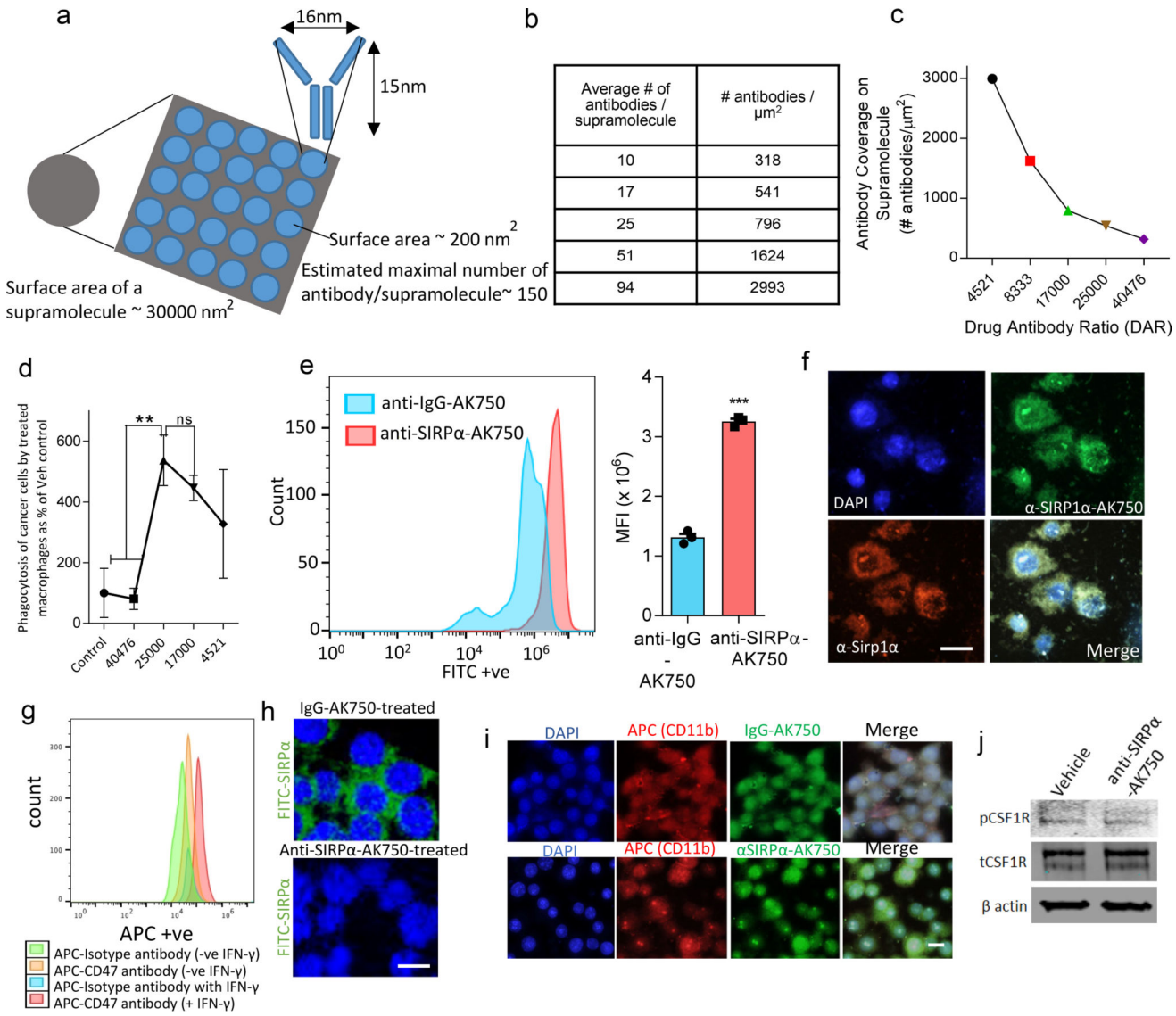


**Figure 5. Engineering a bifunctional anti-SIRPα-AK750 that blocks CD47-SIRPα axis and CSF-1R**

**(a)** Schematic shows the theoretical model of the total surface area of a 100 nm supramolecule and maximal number of antibodies that can be accommodated on the surface. **(b)** Table shows the total number of antibodies on a ~100 nm supramolecule and the corresponding surface density. **(c)** The effect of increasing antibody concentration on the DAR. **(d)** The effect of treatment with supramolecules with increasing antibody concentration but constant number of CSF-1R-inhibiting amphiphiles on the phagocytosis of cancer cells by macrophages. RAW264.7 macrophages were stimulated with IL4 to first generate M2 phenotype, and then incubated with anti-SIRPα-AK750. After 12h incubation, CFSE-labeled B16/F10 melanoma cells were added to the culture, and incubated for 8h. Nuclei were stained with DAPI (blue). Macrophages were labeled with APC-anti-CD11b antibody. AK750 was used as the control arm, and data shown are mean ± SD % change from AK750-treated group (n=3). **(e)** Representative FACS data shows increased binding of

fluorophore-tagged anti-SIRPα-AK750 on TAMs as compared to control isotype IgG-AK750. The TAMs were isolated from the tumors of B16/F10 melanoma tumor bearing mice using CD11b isolation kit. The macrophages were incubated with either FITC- tagged anti-SIRPα-AK750 or control FITC-tagged anti-IgG-AK750 for 4h, followed by washing with cold PBS. Binding of the supramolecules was analyzed using FACS. Graph shows the quantification of the binding and internalization of anti-SIRPα-AK750 to TAMs compared to control anti-IgG-AK750, as measured by mean fluorescence intensity (MFI) in TAMs. Data shown are mean ± SEM (n=3). ***P<0.001 (Student's T test, two-sided). **(f)** Representative confocal images show binding of FITC- tagged anti-SIRPα-AK750 to SIRPα protein on M2 macrophages with anti-SIRPα-AK750. M2 macrophages were generated by stimulating RAW264.7 cells with IL4 followed by incubation with FITC-tagged anti-SIRPα-AK750 for 4h. Nuclei were stained with DAPI (blue) and SIRPα protein was labeled with APC-anti-SIRPα antibody. **(g)** Melanoma cells were treated with interferon gamma (IFNγ) to increase the expression of CD47 as seen using the FACS plot. (h) The CD47-expressing cancer cells were incubated with fluorescently tagged SIRPα in the presence of anti-SIRPα-AK750 or control IgG-AK750. Confocal imaging reveals that the treatment with anti-SIRPα-AK750 completely inhibits the SIRPα-CD47 binding unlike the control IgG-AK750 supramolecules. **(i)** Representative fluorescence images show internalization of FITC- tagged anti-SIRPα-AK750 in M2 macrophages. **(j)** Western blot shows treatment with anti-SIRPα-AK750 decreases the levels of phosphor-CSF-1R without any change to total CSF-1R. Actin levels were used for normalization. RAW264.7 Cells were stimulated with IL4 to generate M2 phenotype, followed by incubation with anti-SIRPα-AK750. After 48h of incubation, the cells were lysed and analyzed using Western blotting. The cropped blots are used in the figure, and full-length blots are presented in Supplementary Fig. 15.

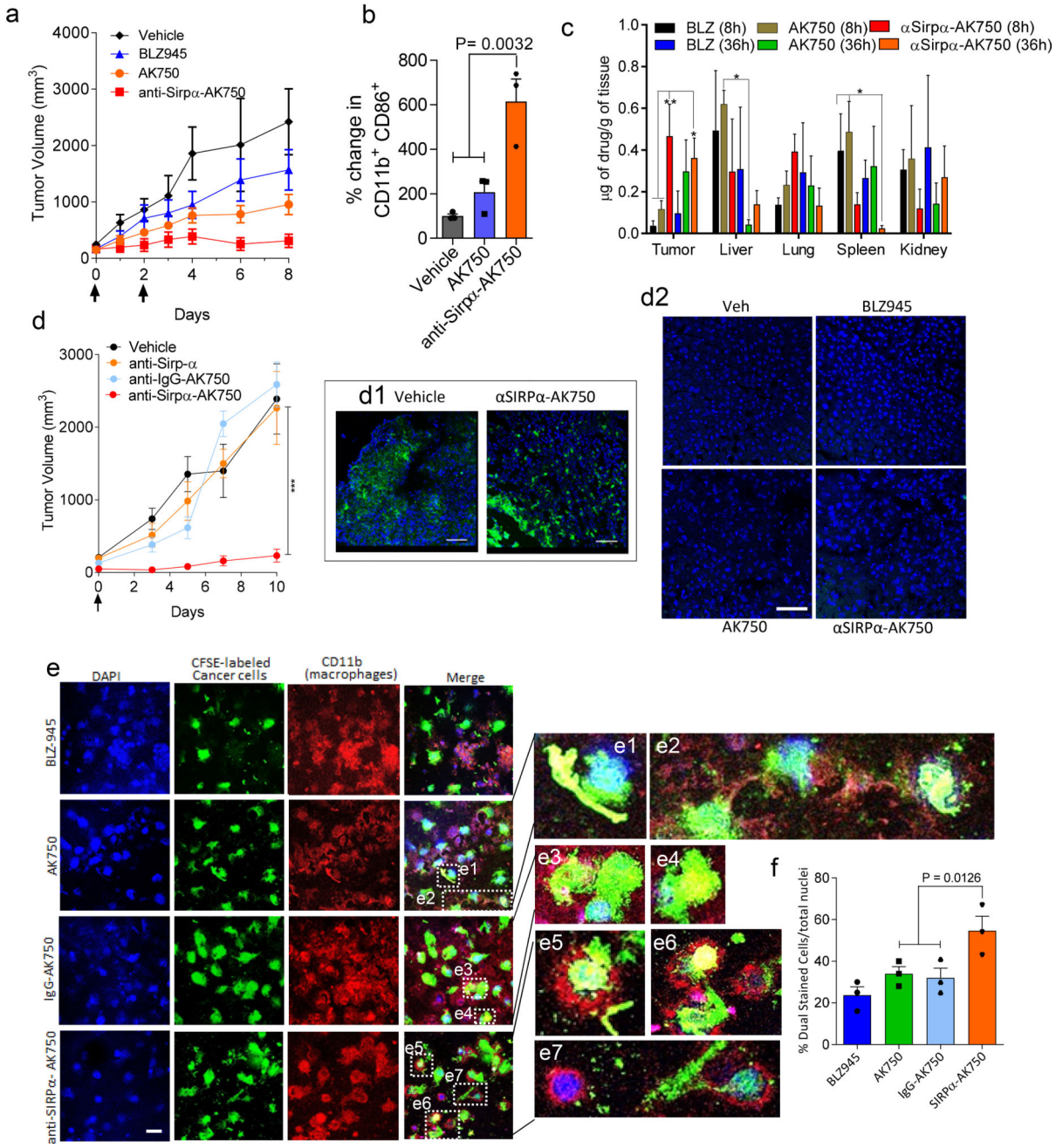


**Fig.6. Single dose of anti-SIRPα-AK750 abrogates tumor growth in a syngeneic B-16/F10 melanoma C57BL/6 mouse model**

**(a)** Tumor growth curves show effect of two cycles of treatments on tumor volume in a syngeneic B-16/F10 melanoma C57BL/6 mice model. Animal with 75 $mm^3$ tumors were randomized into four treatment groups: (1) vehicle controls, (2) BLZ945 (45mg/kg, i.p.), (3) AK750 (mole equivalent to BLZ945 dose), and (4) anti-SIRPα-AK750 (at mole equivalent to BLZ945 dose). One should note the different routes of administration, and i.p. administration can result in lower bioavailability than i.v. administration. First day of treatment was considered as Day 0. Data shown are mean ± SEM (n = 5), *p < 0.05 (One-way ANOVA). **(b)** Graphs show the quantification of expression M1 markers (CD11b

+CD86+) in single cell suspension of the harvested tumor post-treatment, as quantified using flow cytometry. Tumors were harvested on day 10 and single cell suspension was prepared. Data shown are mean ± SEM (n = 3), P value is shown in the graph (One-way ANOVA). **(c)** Graph shows quantitative analysis of drug biodistribution in different organs. Major RES organs were excised from tumor-bearing mice at different time points after a single injection of AK750, anti Sirpα-AK750 and BLZ945. (all animals were dosed with drugs at molar equivalent to 15mg/kg dose of BLZ945, administered I.V.). The drug concentrations per gram of tissue were quantified using LC/MS/MS. Error bars represent mean ± SEM (n=3) (One-way ANOVA). **(d)** Tumor growth curves show effect of a single cycle of treatment on tumor volume in a syngeneic B-16/F10 melanoma C57BL/6 mice model. Animal with 75 $mm^3$ tumors were randomized into four treatment groups: (1) vehicle controls, (2) anti-SIRPα IgG (5mg/kg), (3) IgG-AK750 (equivalent to molar dose equivalent to 45mg/kg of BLZ945), and (4) anti-SIRPα-AK750 (at mole equivalent to AK750 dose used in group 3). Day of treatment was considered as Day 0. Data shown are mean ± SEM (n = 5), ***p < 0.001 (One-way ANOVA). (**d1**) Representative fluorescence images shows $F4/80^+$ macrophages in cross-sections of tumor tissue from vehicle- and anti-SIRPα-AK750-treated groups. (**d2**) Cross sections of liver stained for apoptosis signal (TUNEL) show the absence of any toxicity signal. **(e)** Representative confocal images show the effect of different treatments on phagocytosis of B16/F10 melanoma cells in a co-culture assay with macrophages. RAW264.7 Cells were stimulated with IL4 to generate M2 phenotype, and then incubated with BLZ-945, AK750, IgG-AK750 or anti-SIRPα-AK750 or. After 12h incubation, CFSE-labeled B16/F10 melanoma cells were added to the culture, and incubated for 8h. Nuclei were stained with DAPI (blue), Macrophages were labeled with APC-anti-CD11b antibody. Images were captured using a confocal microscope at same magnification (bar=10 μm). (e1–e7) Zoomed images from corresponding merged images show CFSE-labeled cancer cells (green) being phagocytosed by macrophages (red). **(h)** Graph shows the percentage of phagocytosis as determined by measuring the percentage of dual stained cells (red and green) to total nuclei (blue). Data shown are mean ± SEM (n = 3), p value is shown in the graph (One-way ANOVA followed by Newman Keul's post hoc test).